Two-Dimensional Nanosheets Produced by Liquid Exfoliation of Layered Materials

Jonathan N. Coleman,[1]* Mustafa Lotya,[1] Arlene O'Neill,[1] Shane D. Bergin,[1,6] Paul J. King,[1] Umar Khan,[1] Karen Young,[1] Alexandre Gaucher,[1] Sukanta De,[1] Ronan J. Smith,[1] Igor V. Shvets,[1] Sunil K. Arora,[1] George Stanton,[1] Hye-Young Kim,[2,3] Kangho Lee,[2,3] Gyu Tae Kim,[3] Georg S. Duesberg,[2] Toby Hallam,[2] John J. Boland,[2] Jing Jing Wang,[1] John F. Donegan,[1] Jaime C. Grunlan,[4] Gregory Moriarty,[4] Aleksey Shmeliov,[5] Rebecca J. Nicholls,[5] James M. Perkins,[6] Eleanor M. Grieveson,[5] Koenraad Theuwissen,[5] David W. McComb,[6] Peter D. Nellist,[5] Valeria Nicolosi[5]*

If they could be easily exfoliated, layered materials would become a diverse source of two-dimensional crystals whose properties would be useful in applications ranging from electronics to energy storage. We show that layered compounds such as MoS_2, WS_2, $MoSe_2$, $MoTe_2$, $TaSe_2$, $NbSe_2$, $NiTe_2$, BN, and Bi_2Te_3 can be efficiently dispersed in common solvents and can be deposited as individual flakes or formed into films. Electron microscopy strongly suggests that the material is exfoliated into individual layers. By blending this material with suspensions of other nanomaterials or polymer solutions, we can prepare hybrid dispersions or composites, which can be cast into films. We show that WS_2 and MoS_2 effectively reinforce polymers, whereas WS_2/carbon nanotube hybrid films have high conductivity, leading to promising thermoelectric properties.

Layered materials represent a diverse and largely untapped source of two-dimensional (2D) systems with exotic electronic properties and high specific surface areas that are important for sensing, catalysis, and energy storage applications. Although graphene is the most well-known layered material, transition metal dichalcogenides (TMDs), transition metal oxides (TMOs), and other 2D compounds such as BN, Bi_2Te_3, and Bi_2Se_3 are also important. The latter materials are of particular interest as topological insulators and thermoelectric materials (*1*). However, the development of these materials has been hampered by the lack of a simple method to exfoliate them to give mono- or few-layer flakes in large quantities.

TMDs consist of hexagonal layers of metal atoms (M) sandwiched between two layers of chalcogen atoms (X) with stoichiometry MX_2. Although the bonding within these trilayer sheets is covalent, adjacent sheets stack via van der Waals interactions to form a 3D crystal. TMDs occur in more than 40 different types (*2*, *3*), depending on the combination of chalcogen (S, Se, or Te) and transition metal (*3*). Depending on the coordination and oxidation state of the metal atoms, TMDs can be metallic, semimetallic, or semiconducting (*2*, *3*); for example, WS_2 is a semiconductor, whereas $NbSe_2$ is a metal (*3*). In addition, superconductivity (*4*) and charge-density wave effects (*5*) have been observed in some TMDs. This versatility makes them potentially useful in many areas of electronics.

However, like graphene (*6*), layered materials must be exfoliated to fulfil their full potential. For example, films of exfoliated Bi_2Te_3 should display enhanced thermoelectric efficiency by suppression of thermal conductivity (*7*). Exfoliation of 2D topological insulators such as Bi_2Te_3 and Bi_2Se_3 would reduce residual bulk conductance, highlighting surface effects. In addition, we can expect changes in electronic properties as the number of layers is reduced; for instance, the indirect band gap of bulk MoS_2 becomes direct in few-layer flakes (*8*). Although exfoliation can be achieved mechanically on a small scale (*9*, *10*), liquid-phase exfoliation methods are required for many applications (*11*). A simple liquid exfoliation method would allow the formation of novel hybrid and composite materials. Although TMDs can be chemically exfoliated in liquids (*12*–*14*), this method is time-consuming, extremely sensitive to the environment, and incompatible with most solvents.

We demonstrated exfoliation of bulk TMD crystals in common solvents to give mono- and few-layer nanosheets. This method is insensitive to air and water and can potentially be scaled up to give large quantities of exfoliated material. In addition, we showed that this procedure allows the formation of hybrid films with enhanced properties.

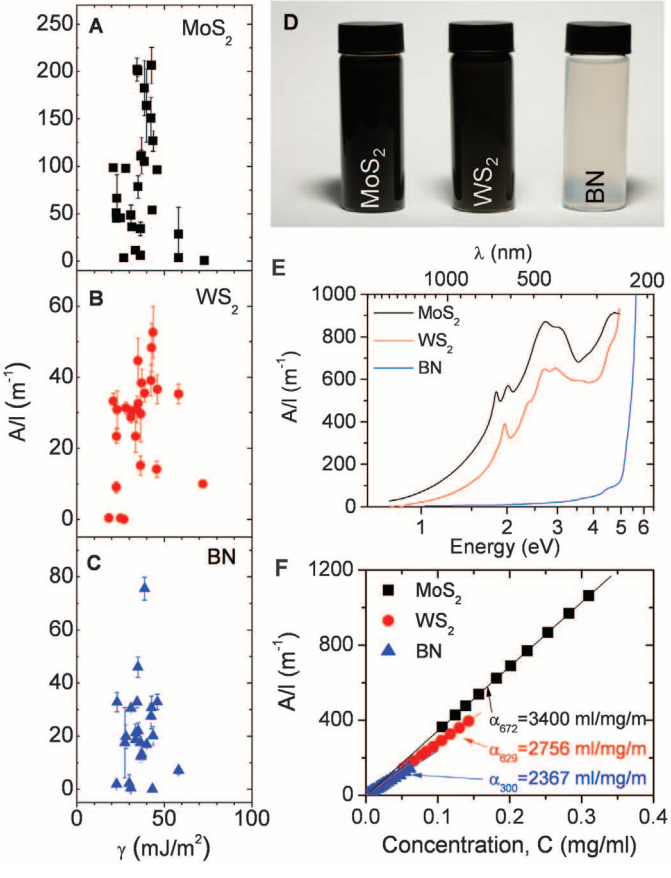

Fig. 1. Optical characterization of nanosheet dispersions. (**A** to **C**) Concentration remaining after centrifugation (plotted as *A*/*l*) for MoS_2, WS_2, and BN dispersed in a range of solvents, plotted versus solvent surface tension, γ. (**D**) Photographs of dispersions of MoS_2 (in NMP), WS_2 (in NMP), and BN (in IPA). (**E**) Absorbance spectra of dispersions of MoS_2 (NMP, 0.16 mg/ml), WS_2 (NMP, 0.15 mg/ml), and BN (IPA, 0.002 mg/ml). (**F**) Lambert-Beer plots for MoS_2 (NMP), WS_2 (NMP), and BN (IPA). The dispersions in (D) to (F) were prepared using optimized dispersion conditions (*25*).

[1]School of Physics and Centre for Research on Adaptive Nanostructures and Nanodevices (CRANN), Trinity College Dublin, D2, Ireland. [2]School of Chemistry and CRANN, Trinity College Dublin, D2, Ireland. [3]School of Electrical Engineering, Korea University, Seoul, South Korea. [4]Department of Mechanical Engineering, Texas A&M University, College Station, TX 77843, USA. [5]Department of Materials, University of Oxford, Parks Road, Oxford OX1 3PH, UK. [6]Department of Materials, Imperial College London, London SW7 2AZ, UK.

*To whom correspondence should be addressed. E-mail: colemaj@tcd.ie (J.N.C.); valeria.nicolosi@materials.ox.ac.uk (V.N.)

We initially sonicated commercial MoS_2, WS_2, and BN (*15*, *16*) powders in a number of solvents with varying surface tensions (see sections S1 and S2 in the supporting online material for methods). The resultant dispersions were centrifuged, and the supernatant was decanted (section S3). Optical absorption spectroscopy showed that the amount of material retained (characterized by $A/l = \alpha C$, where A/l is the absorbance per length, α is the extinction coefficient, and C is the concentration) was maximized for solvents with surface tension close to γ-40 mJ/m^2 (*17*, *18*) (Fig. 1, A to C). Detailed analysis, within the framework of Hansen solubility parameter theory (*19*), shows successful solvents to be those with dispersive, polar, and H-bonding components of the cohesive energy density within certain well-defined ranges (section S4 and figs. S2 and S3). This can

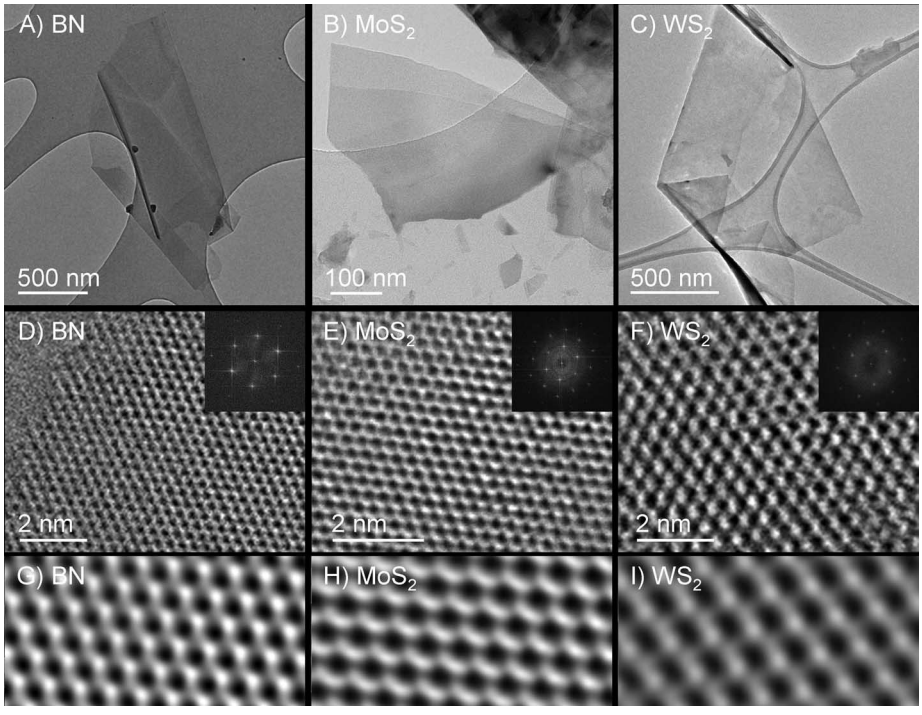

Fig. 2. TEM of nanosheets. (**A** to **C**) Low-resolution TEM images of flakes of BN, MoS_2, and WS_2, respectively. (**D** to **F**) High-resolution TEM images of BN, MoS_2, and WS_2 monolayers. (Insets) Fast Fourier transforms of the images. (**G** to **I**) Butterworth-filtered images of sections of the images in (D) to (F).

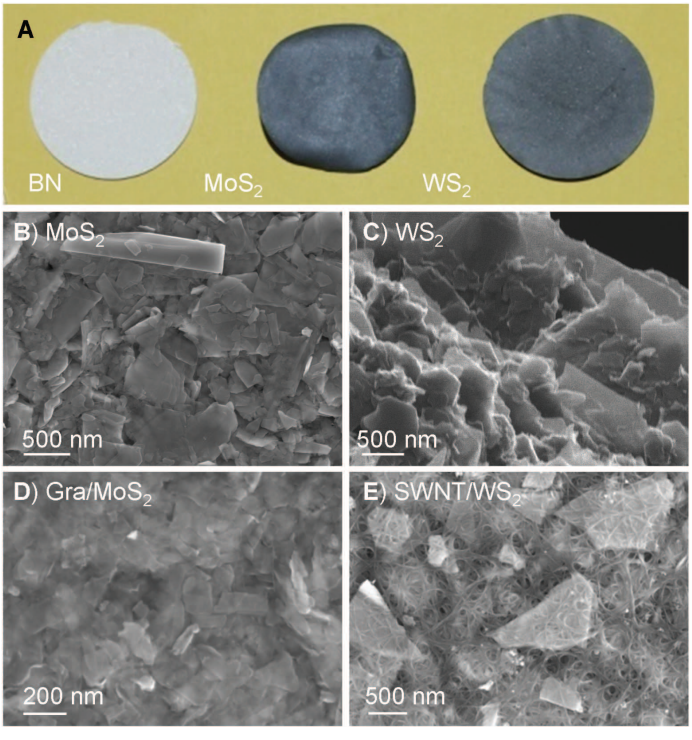

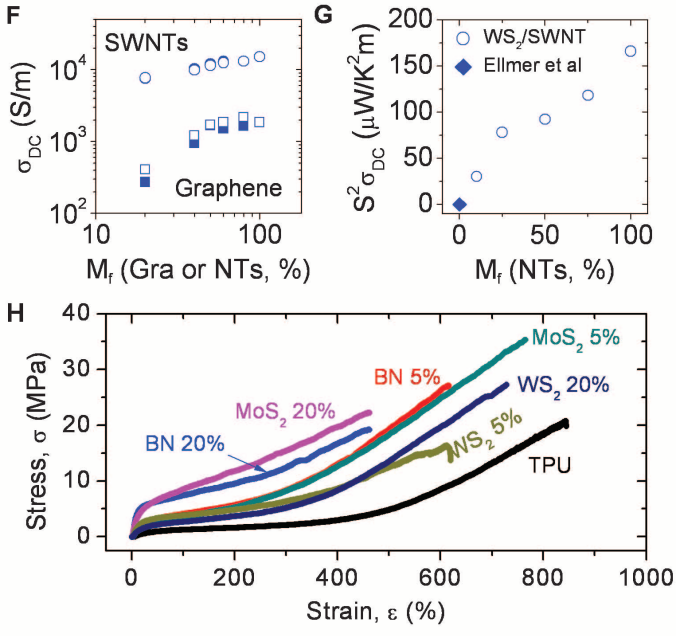

Fig. 3. Nanosheet films, hybrids, and composites. (**A**) Photograph of free-standing films of BN, MoS_2, and WS_2 (thickness ~ 50 μm). (**B**) An SEM image of the surface of a MoS_2 film. (**C**) He ion microscope image of the edge of a WS_2 film. (**D** and **E**) SEM images of the surface of a graphene/MoS_2 hybrid film and a SWNT/ WS_2 hybrid film, respectively. (**F**) dc conductivity of thin (~200 nm) hybrid films prepared from mixtures of WS_2 or MoS_2 (open or solid symbols) and SWNTs or graphene (Gra) (circles or squares) as a function of filler mass fraction, M_f. (**G**) Product of S coefficient squared and dc conductivity (the power factor) for thick (~50 μm) WS_2/SWNT hybrid films as a function of nanotube mass fraction. Although the WS_2 film proved too brittle to measure, Ellmer *et al*. measured $S^2\sigma = 0.22$ μW/K^{2}m for a disordered WS_2 film. (**H**) Representative stress-strain curves for composites of thermoplastic polyurethane (TPU) filled with each layered compound at loading levels of 5 weight percent (wt %) and 20 wt %.

be interpreted to mean that successful solvents are those that minimize the energy of exfoliation. This information will facilitate the search for new solvents and the development of solvent blends. Some of the more promising solvents were *N*-methyl-pyrrolidone (NMP) and isopropanol (IPA) (see table S1 for the full solvent list). Optimization of the dispersion procedure (section S5) gave concentrations as high as 0.3 mg/ml for MoS_2, 0.15 mg/ml for WS_2 (both in NMP), and 0.06 mg/ml for BN (IPA). Photographs of typical dispersions, which are stable over periods of hundreds of hours (section S8 and fig. S13), are shown in Fig. 1D. Optical absorption spectra (Fig. 1E) show features expected for MoS_2 and WS_2 (*20*, *21*). In addition, a band edge at ~5 eV is clearly observed for dispersed BN. However, the spectra appear to be superimposed on a background, possibly because of scattering (section S6 and fig. S4). A/l scaled linearly with C for all samples, allowing calculation of α values (Fig. 1F).

We performed transmission electron microscopy (TEM) analysis on our dispersions, typically observing 2D flakes consisting of thin nanosheets. Examples of very thin sheets observed for all three materials are shown in Fig. 2, A to C. The lateral size of these objects was typically 50 to 1000 nm for MoS_2 and WS_2 and 100 to 5000 nm for BN (section S7 and figs. S5 to S12). We could examine these objects in more detail using aberration-corrected TEM (Fig. 2, D to F). These images and associated Fourier transforms illustrate the hexagonal symmetry of these materials. This is in contrast to reports on MoS_2 and WS_2 exfoliated by lithium intercalation, which results in substantial deviation from hexagonal structure (*22*–*24*). Figure 2, G to I, show sections of the images in Fig. 2, D to F, after low-pass Butterworth filtering was performed. These images reveal B-N bond lengths of 1.45 Å and MoS_2 and WS_2 hexagon widths of 3.8 Å and 4 Å, confirming that no distortions were introduced by exfoliation. Analysis of TEM intensity profiles, coupled with flake-edge analysis, electron diffraction data, and EELS data, suggests the presence of monosheets in the sample (*25*).

Our dispersion/exfoliation method allowed us to prepare films of BN, MoS_2, and WS_2 by vacuum filtration (*17*) or spraying, with thickness ranging from a few nanometers to hundreds of micrometers. Photographs of free-standing films are shown in Fig. 3A. Scanning electron and helium ion microscopy of the surface and edges of these films show them to consist of partially aligned 2D platelets (Fig. 3, B and C, and fig. S17). The versatility of the solvent-exfoliation method makes it easy to create hybrid dispersions and films by simply adding another material to the dispersion. We illustrated this by preparing hybrid dispersions and so films of MoS_2 or WS_2 mixed with graphene or single-walled nanotubes (SWNTs) (Fig. 3, D and E, and section S10). With the exception of pure BN, all films were mechanically robust (section S10 and figs. S18 and S20). The addition of graphene or SWNTs increased the dc conductivity, σ_{dc}, from ~10^{-6} S/m for the TMD-only films to ~2×10^4 S/m for the SWNT-based hybrids (Fig. 3F). We performed thermoelectric measurements on free-standing WS_2/SWNT hybrid films, measuring σ_{dc} and the Seebeck coefficient, S. Obtaining significant increases in σ_{dc} without degrading S to give a high power factor ($S^2\sigma_{dc}$) is critically important in thermoelectric research (*26*). Here, $S^2\sigma_{dc}$ increased from 0.2 $\mu W/K^2m$ for disordered WS_2 films (*27*) to >100 $\mu W/K^2m$ for WS_2/SWNT films (Fig. 3G and section S10).

Solvent processing greatly simplifies composite preparation (*28*–*31*), allowing us to prepare composites of thermoplastic polyurethane filled with BN, MoS_2, and WS_2. We observed substantial levels of reinforcement, comparable to the best results achieved using graphene (*32*) or nanoclays (*33*) as fillers (Fig. 3H and figs. S19 and S20).

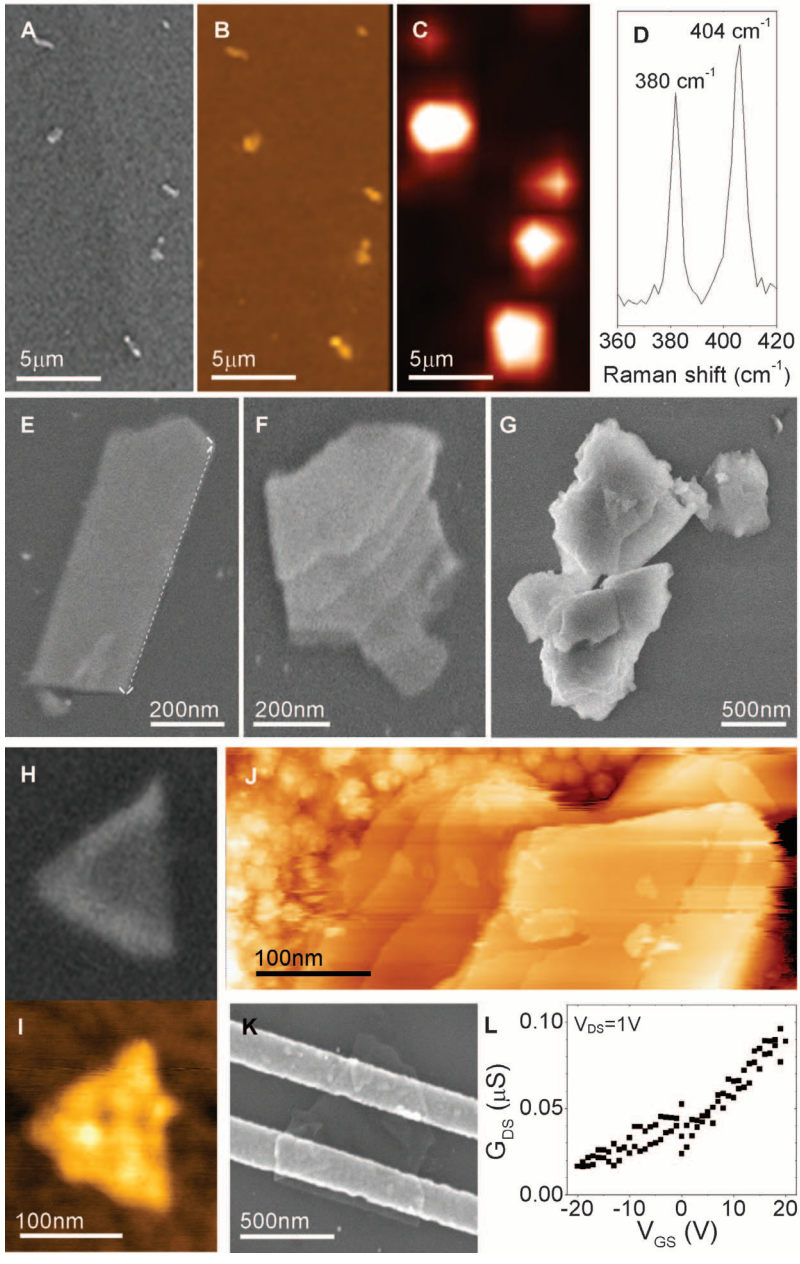

Fig. 4. Deposition of nanosheets onto surfaces. (**A** and **B**) An SEM and an AFM image of MoS_2 flakes deposited on SiO_2 by spraying. (**C**) A Raman map of the same region. (**D**) Typical Raman spectrum of an individual flake. The Raman map plots the integral of the spectrum between 390 and 410 cm^{-1}. (**E** to **G**) A very thin flake, a multilayer, and a cluster of aggregated multilayers. The dashed line in (E) has been inserted to illustrate the straightness of the flake edge. (**H** and **I**) SEM and AFM images of an individual flake. (**J**) An STM image of an individual flake. The flakes in (I) and (J) have heights of 5 and 10 nm, respectively (*25*). (**K**) An SEM image of an MoS_2 flake on Si/SiO_2 with electrodes deposited on top. (**L**) Drain-source conductance (G_{DS}) as a function of gate voltage (V_{GS}) for the flake shown in (K). V_{DS} is the applied drain-source voltage.

Exfoliated flakes can be deposited on substrates by spraying. Shown in Fig. 4, A and B, are a scanning electron microscopy (SEM) and an atomic force microscopy (AFM) image of a silicon wafer spray-coated with MoS_2. The objects observed are hundreds of nanometers wide, in agreement with the TEM data (*25*). We can confirm that the flakes consist of MoS_2 by Raman mapping (Fig. 4C), based on the individual flake spectrum shown in Fig. 4D. The peak positions (*25*, *34*) in Fig. 4D are consistent with trigonal prismatic (2H) mono- or bilayer MoS_2 (section S9). SEM analysis (Fig. 4, E to H) shows that although some deposited flakes are very thin, many are multilayers or clusters that have aggregated during deposition. AFM and STM imaging of individual flakes show them to display typical thicknesses of ~3 to 12 nm (Fig. 4, I and J; figs. S15 and S16; and section S9). Some of these images, particularly the STM image in Fig. 4J, show steps. These are consistently ~1 nm high and probably originate in layer edges. Electrical characterization of individual flakes shows n-type field-effect behavior characterized by mobilities of ~0.01 cm^2/Vs (*9*, *10*), which is rather lower than observed for mechanically exfoliated MoS_2 flakes (Fig. 4, K and L, and section S11).

This exfoliation process is not limited to BN, MoS_2, and WS_2. We have exfoliated $MoSe_2$, $MoTe_2$, $TaSe_2$, $NbSe_2$, $NiTe_2$, and Bi_2Te_3 in a number of the solvents listed in table S1 (section S12 and figs. S23 and S24) and believe that similar solvents may exfoliate all MX_2 compounds. We propose that this exfoliation technique is general, as it can be applied to TMDs, graphene, BN, and Bi_2Te_3. As such, we expect to extend it to TMOs (*35*) and other layered compounds.

References and Notes

1. S. K. Mishra, S. Satpathy, O. Jepsen, *J. Phys. Condens. Matter* **9**, 461 (1997).
2. E. A. Marseglia, *Int. Rev. Phys. Chem.* **3**, 177 (1983).
3. J. A. Wilson, A. D. Yoffe, *Adv. Phys.* **18**, 193 (1969).
4. F. R. Gamble, B. G. Silbernagel, *J. Chem. Phys.* **63**, 2544 (1975).
5. F. Clerc *et al.*, *J. Phys. Condens. Matter* **19**, 355002 (2007).
6. A. K. Geim, *Science* **324**, 1530 (2009).
7. B. Poudel *et al.*, *Science* **320**, 634 (2008).
8. A. Splendiani *et al.*, *Nano Lett.* **10**, 1271 (2010).
9. K. S. Novoselov *et al.*, *Proc. Natl. Acad. Sci. U.S.A.* **102**, 10451 (2005).
10. A. Ayari, E. Cobas, O. Ogundadegbe, M. S. Fuhrer, *J. Appl. Phys.* **101**, 014507 (2007).
11. R. Ruoff, *Nat. Nanotechnol.* **3**, 10 (2008).
12. P. Joensen, R. F. Frindt, S. R. Morrison, *Mater. Res. Bull.* **21**, 457 (1986).
13. C. Liu, O. Singh, P. Joensen, A. E. Curzon, R. F. Frindt, *Thin Solid Films* **113**, 165 (1984).
14. H. Matte *et al.*, *Angew. Chem. Int. Ed.* **49**, 4059 (2010).
15. A. Nag *et al.*, *ACS Nano* **4**, 1539 (2010).
16. C. Y. Zhi, Y. Bando, C. C. Tang, H. Kuwahara, D. Golberg, *Adv. Mater.* **21**, 2889 (2009).
17. Y. Hernandez *et al.*, *Nat. Nanotechnol.* **3**, 563 (2008).
18. S. D. Bergin *et al.*, *Adv. Mater.* **20**, 1876 (2008).
19. S. D. Bergin *et al.*, *ACS Nano* **3**, 2340 (2009).
20. E. A. Ponomarev, M. Neumann-Spallart, G. Hodes, C. Lévy-Clément, *Thin Solid Films* **280**, 86 (1996).
21. J. P. Wilcoxon, P. P. Newcomer, G. A. Samara, *J. Appl. Phys.* **81**, 7934 (1997).
22. R. Bissessur, M. G. Kanatzidis, J. L. Schindler, C. R. Kannewurf, *J. Chem. Soc. Chem. Commun.* **1993** 1582 (1993).
23. G. L. Frey, K. J. Reynolds, R. H. Friend, H. Cohen, Y. Feldman, *J. Am. Chem. Soc.* **125**, 5998 (2003).
24. R. A. Gordon, D. Yang, E. D. Crozier, D. T. Jiang, R. F. Frindt, *Phys. Rev. B* **65**, 125407 (2002).
25. See supporting material on *Science* Online.
26. M. S. Dresselhaus *et al.*, *Adv. Mater.* **19**, 1043 (2007).
27. K. Ellmer, C. Stock, K. Diesner, I. Sieber, *J. Cryst. Growth* **182**, 389 (1997).
28. E. Benavente, M. A. S. Ana, G. González, *Phys. Status Solidi B* **241**, 2444 (2004).
29. R. F. Frindt, D. Yang, *Mol. Cryst. Liquid Cryst. Sci. Technol. Sect. A Mol. Cryst. Liquid Cryst.* **311**, 367 (1998).
30. J. P. Lemmon, J. H. Wu, C. Oriakhi, M. M. Lerner, *Electrochim. Acta* **40**, 2245 (1995).
31. B. H. Xu, B. Z. Lin, D. Y. Sun, C. Ding, *Electrochim. Acta* **52**, 3028 (2007).
32. U. Khan, P. May, A. O'Neill, J. N. Coleman, *Carbon* **48**, 4035 (2010).
33. S. M. Liff, N. Kumar, G. H. McKinley, *Nat. Mater.* **6**, 76 (2007).
34. C. Lee *et al.*, *ACS Nano* **4**, 2695 (2010).
35. M. Osada, T. Sasaki, *J. Mater. Chem.* **19**, 2503 (2009).

36. The authors acknowledge the Irish Research Council for Science, Engineering & Technology (Embark Initiative), the European Research Council, and Science Foundation Ireland (grant number 07/IN.7/I1772) for financial support. V.N. acknowledges funding from the Marie Curie grant PIEF-GA-2008-220150 and the Royal Academy of Engineering/Engineering and Physical Sciences Research Council and thanks BegbrokeNano for their provision of research facilities.

Supporting Online Material

www.sciencemag.org/cgi/content/full/331/6017/568/DC1
Materials and Methods
SOM Text
Figs. S1 to S24
Tables S1 to S4
References

12 July 2010; accepted 7 January 2011
10.1126/science.1194975

Protein Native-State Stabilization by Placing Aromatic Side Chains in N-Glycosylated Reverse Turns

Elizabeth K. Culyba,[1,2]* Joshua L. Price,[1,2]* Sarah R. Hanson,[1,2] Apratim Dhar,[3] Chi-Huey Wong,[1,2] Martin Gruebele,[4] Evan T. Powers,[1,2]† Jeffery W. Kelly[1,2,5]†

N-glycosylation of eukaryotic proteins helps them fold and traverse the cellular secretory pathway and can increase their stability, although the molecular basis for stabilization is poorly understood. Glycosylation of proteins at naïve sites (ones that normally are not glycosylated) could be useful for therapeutic and research applications but currently results in unpredictable changes to protein stability. We show that placing a phenylalanine residue two or three positions before a glycosylated asparagine in distinct reverse turns facilitates stabilizing interactions between the aromatic side chain and the first *N*-acetylglucosamine of the glycan. Glycosylating this portable structural module, an enhanced aromatic sequon, in three different proteins stabilizes their native states by −0.7 to −2.0 kilocalories per mole and increases cellular glycosylation efficiency.

In eukaryotic cells, N-glycosylation occurs cotranslationally as the ribosome inserts proteins into the endoplasmic reticulum (ER). The oligosaccharyl transferase (OST) attaches the $Glc_3Man_9GlcNAc_2$ (where Glc, Man, and GlcNAc are glucose, mannose, and *N*-acetylglucosamine, respectively) oligosaccharide to the Asn side chain within some Asn-Xxx-Thr/Ser sequons (where Xxx denotes any amino acid except Pro and the slash indicates "or") (*1*). The factors governing glycosylation efficiency are incompletely understood. Asn-linked glycans extrinsically affect protein-folding efficiency in the ER because the glycan tag can direct the protein into the calnexin and/or calreticulin (CNX/CRT) folding versus degradation pathway (*2*, *3*). Glycans can also intrinsically stabilize proteins (*4*–*11*).

Protein stabilization through N-glycosylation decreases the population of the aggregation-prone, protease-sensitive unfolded state relative to the folded ensemble, increasing serum half-life, improving shelf-life, and shielding immunogenic epitopes (*12*). Conferring these properties by adding N-glycans to naïve proteins (not normally glycosylated) or to glycoproteins at naïve sites could have useful applications. However, attempts to add N-glycans to proteins by trial and error have had unpredictable thermodynamic consequences and often led to destabilization (*13*–*15*). Thus, we sought an increased understanding of glycan-protein interactions that mediate

[1]Department of Chemistry, The Scripps Research Institute, La Jolla, CA 92037, USA. [2]The Skaggs Institute for Chemical Biology, The Scripps Research Institute, La Jolla, CA 92037, USA. [3]Department of Chemistry, University of Illinois, Urbana, IL 61801, USA. [4]Center for Biophysics and Computational Biology and Departments of Chemistry and Physics, University of Illinois, Urbana, IL 61801, USA. [5]Department of Molecular and Experimental Medicine, The Scripps Research Institute, La Jolla, CA 92037, USA.

*These authors contributed equally to this work.
†To whom correspondence should be addressed. E-mail: epowers@scripps.edu (E.T.P.); jkelly@scripps.edu (J.W.K.)